

# A mathematical model and inversion procedure for Magneto-Acousto-Electric Tomography (MAET)

Leonid Kunyansky

**Abstract.** Magneto-Acousto-Electric Tomography (MAET), also known as the Lorentz force or Hall effect tomography, is a novel hybrid modality designed to be a high-resolution alternative to the unstable Electrical Impedance Tomography. In the present paper we analyze existing mathematical models of this method, and propose a general procedure for solving the inverse problem associated with MAET. It consists in applying to the data one of the algorithms of Thermo-Acoustic tomography, followed by solving the Neumann problem for the Laplace equation and the Poisson equation.

For the particular case when the region of interest is a cube, we present an explicit series solution resulting in a fast reconstruction algorithm. As we show, both analytically and numerically, MAET is a stable technique yielding high-resolution images even in the presence of significant noise in the data.

Department of Mathematics, University of Arizona, Tucson, AZ 85721, USA

E-mail: [leonk@math.arizona.edu](mailto:leonk@math.arizona.edu)

AMS classification scheme numbers: 44A12, 92C55, 65R32

*Keywords:* Magneto-Acousto-Electric tomography, spherical means, time reversal, explicit inversion formulae, synthetic focusing

## Introduction

Magneto-Acousto-Electric Tomography (MAET) is based on the measurements of the electrical potential arising when an acoustic wave propagates through conductive medium placed in a constant magnetic field [26, 34]. The interaction of the mechanical motion of the free charges (ions and/or electrons) with the magnetic field results in the Lorentz force that causes separation of charges and, thus, generates Lorentz currents within the tissue. The goal of MAET coincides with that of the Electrical Impedance Tomography (EIT): to reconstruct the conductivity of the tissue from the values of the electric potential measured on the boundary of the object. EIT is a fast, inexpensive, and harmless modality, which is potentially very valuable due to the large contrast in the conductivity between healthy and cancerous tissues [5, 6, 9]. Unfortunately, the reconstruction problems arising in EIT are known to be exponentially unstable.

MAET is one of the several recently introduced hybrid imaging techniques designed to stabilize the reconstruction of electrical properties of the tissues by coupling together ultrasound waves with other physical phenomena. Perhaps the best known examples

of hybrid methods are the Thermo-Acoustic Tomography (TAT) [16] and the closely related Photo-Acoustic modality, PAT [15, 29]). In the latter methods the amount of electromagnetic energy absorbed by the medium is reconstructed from the measurements (on the surface of the object) of acoustic waves caused by the thermoacoustic expansion (see e.g. [17, 33]). Another hybrid technique, designed to overcome the instability of EIT is Acousto-Electric Impedance Tomography (AEIT) [36]. It couples together acoustic waves and electrical currents, through the electroacoustic effect (see [25]). Although AEIT has been shown, both theoretically and in numerical simulations, to be stable and capable of yielding high-resolution images [3, 8, 18, 19], the feasibility of practical reconstructions is still in question due to the weakness of the acousto-electric effect.

In the present paper we analyze MAET, a modality designed to stably reconstruct the conductivity by combining magnetic field, acoustic excitation and electric measurements, coupled through the Lorentz force. The physical foundations of MAET were established in [26] and [34]. It was shown ([26]) that if the tissue with conductivity  $\sigma(x)$  moves with velocity  $V(x, t)$  within the constant magnetic field  $B$ , the arising Lorentz force will generate Lorentz currents  $J_L(x, t)$  given by the following formula

$$J_L(x, t) = \sigma(x)B \times V(x, t). \quad (1)$$

Originally [26, 34] it was proposed to utilize a focused propagating acoustic pulse to induce the electrical response. In [13] wavepackets of a certain frequency were used in a physical experiment to reconstruct the current density in a thin slab of a tissue. Similarly, in [4] the use of a perfectly focused acoustic beam was assumed in a theoretical study and in numerical simulations. However, in the above-quoted works accurate mathematical model(s) of such beams were not presented. Moreover, the feasibility of focusing a fixed frequency acoustic beam at an arbitrary point inside the 3D body is problematic. In a theoretical study [30] the use of plane waves of varying frequencies was proposed instead of the beams. This is a more realistic approach; however, the analysis in that work relies on several crude approximations (the conductivity is assumed to be close to 1, and the electric field is approximated by one term in the multipole expansion).

To summarize, the existing mathematical models of measurements in MAET are of approximate nature; moreover, some of them contradict to others. For example, it was found in [13] that if one uses a pair of electrodes to measure the voltage (difference of the potentials) at two points  $a$  and  $b$  on the boundary of the body, the result is the integral of the mixed product of three vectors: velocity  $V$ , magnetic induction  $B$  and the so-called lead current  $J_{ab}$  (the current that would flow in the body if the difference of potentials were applied at points  $a$  and  $b$ ). The approximate model in [30] implicitly agrees with this conclusion. However, in [4] it is assumed that if the pulse is focused at the point  $x$ , the measurements will be proportional to the product of the electric potential  $u(x)$  and conductivity  $\sigma(x)$ . This assumption contradicts the previous models; it also seems to be unrealistic since potential  $u(x)$  is defined up to an arbitrary constant, while the measurements are completely determined by the physics of the problem.

In the present paper we first derive, starting from equation (1), a rigorous and

general model of the MAET measurements. Next, we show that if a sufficient amount of data is measured, one can reconstruct, almost explicitly and in a stable fashion the conductivity of the tissue. For general domains the reconstruction can be reduced to the solution of the inverse problem of TAT followed by the solution of the Neumann problem for the Laplace equation, and a Poisson equation. In the simpler case of a rectangular domain the reconstruction formulae can be made completely explicit, and the solution is obtained by summing several Fourier series. In the latter case the algorithm is fast, i.e. it runs in  $O(n^3 \log n)$  floating point operations on a  $n \times n \times n$  grid. The results of numerical simulations show that high resolution images of the conductivity can be stably recovered from MAET measurements even in the presence of a significant noise.

## 1. Formulation of the problem

Suppose that the object of interest whose conductivity  $\sigma(x)$  we would like to recover is supported within an open and bounded region  $\Omega$  with the boundary  $\partial\Omega$ . For simplicity we will assume that  $\sigma(x)$  is smooth in  $\Omega$ , does not approach 0, and equals 1 in the vicinity of  $\partial\Omega$ ; the support of  $\sigma(x) - 1$  lies in some  $\Omega_1 \subset \Omega$  and the distance between  $\Omega_1$  and  $\partial\Omega$  is non-zero. The object is placed in the magnetic field with a constant magnetic induction  $B$ , and an acoustic wave generated by a source lying outside  $\Omega$  propagates through the object with the velocity  $V(x, t)$ . The Lorentz force induces currents  $J_L(x, t)$  in  $\Omega$  given by equation (1). We assume that the electrical interactions occur on much faster time scale than the mechanical ones, and so all currents and electric potentials depend on  $t$  only as a parameter. In addition to Lorentz currents, the arising electrical potential  $u(x, t)$  generates secondary, Ohmic currents  $J_O(x, t)$  given by Ohm's law

$$J_O(x, t) = \sigma(x) \nabla u(x, t).$$

Since there are no sinks or sources of charges in  $\Omega$ , the total current is divergence-free

$$\nabla \cdot (J_L + J_O) = 0.$$

Thus

$$\nabla \cdot \sigma \nabla u = -\nabla \cdot (\sigma B \times V). \quad (2)$$

Since there are no currents through the boundary, the normal component of the total current  $J_L(x, t) + J_O(x, t)$  vanishes:

$$\frac{\partial}{\partial n} u(z) = -(B \times V(z)) \cdot n(z), \quad z \in \partial\Omega, \quad (3)$$

where  $n(z)$  is the exterior normal to  $\partial\Omega$  at point  $z$ .

We will assume that the boundary values of the potential  $u(z, t)$  can be measured at all points  $z$  lying on  $\partial\Omega$ . We will model the measurements by integrating  $u(z, t)$  with a weight  $I(z)$ , thus, forming measuring functional  $M$  defined by the formula

$$M(t) = \int_{\partial\Omega} I(z) u(z, t) dA(z), \quad (4)$$

where  $A(z)$  is the standard area element. Weight  $I(z)$  can be a function or a distribution, subject to the only restriction that its integral over  $\partial\Omega$  equals zero. In particular, if one chooses to use  $I(z) = \delta(z - a) - \delta(z - b)$ , where  $\delta(\cdot)$  is the 2D Dirac delta-function, then  $M$  models the two-point measuring scheme utilized in [13] and [30].

In order to understand what kind of information is encoded in the values of  $M(t)$  let us consider solution  $w_I(x)$  of the following divergence equation

$$\nabla \cdot \sigma \nabla w_I(x) = 0, \quad (5)$$

$$\frac{\partial}{\partial n} w_I(z) = I(z), \quad z \in \partial\Omega. \quad (6)$$

(To ensure the uniqueness we will require that the integral of  $w_I(z)$  over  $\Omega$  vanishes.) Then  $w_I(x)$  equals the electric potential that would be induced in the tissue by injecting currents  $I(z)$  through  $\partial\Omega$ . Let us denote the corresponding currents  $\sigma \nabla w_I(x)$  by  $J_I(x)$ :

$$J_I(x) = \sigma \nabla w_I(x). \quad (7)$$

Let us now apply the second Green's identity to functions  $u(x, t)$ ,  $w_I(x)$ , and  $\sigma(x)$ :

$$\int_{\Omega} [w_I \nabla \cdot (\sigma \nabla u) - u \nabla \cdot (\sigma \nabla w_I)] dx = \int_{\partial\Omega} \sigma \left[ w_I \frac{\partial}{\partial n} u - u \frac{\partial}{\partial n} w_I \right] dA(z). \quad (8)$$

By taking into account (3), (2), (5), and (6), equation (8) can be simplified to

$$- \int_{\Omega} w_I \nabla \cdot (\sigma B \times V) dx = \int_{\partial\Omega} \sigma w_I \frac{\partial}{\partial n} u dA(z) - M(t). \quad (9)$$

By integrating the left side of (9) by parts and by replacing  $\frac{\partial}{\partial n} u$  with (3) one obtains:

$$\begin{aligned} \int_{\Omega} \sigma \nabla w_I \cdot (B \times V) dx - \int_{\partial\Omega} w_I \sigma (B \times V) \cdot n dA(z) &= - \int_{\partial\Omega} \sigma w_I (B \times V) \cdot n dA(z) - M(t), \\ M(t) &= - \int_{\Omega} \sigma \nabla w_I \cdot (B \times V) dx = - \int_{\Omega} J_I \cdot (B \times V) dx = B \cdot \int_{\Omega} J_I(x) \times V(x, t) dx \end{aligned} \quad (10)$$

(Equation (1) in [13] is the particular case of (9) for  $I(z) = \delta(z - a) - \delta(z - b)$ .)

It is clear from equation (10) that MAET measurements recover some information about currents  $J_I(x)$ . Let us assume that the speed of sound  $c$  and density  $\rho$  of the tissues are approximately constant (as happens in breast imaging, one of the most important potential applications). Then acoustic pressure  $p(x, t)$  satisfies the wave equation in  $\Omega$ :

$$\frac{1}{c^2} \frac{\partial^2}{\partial t^2} p(x, t) = \Delta p(x, t). \quad (11)$$

Additionally,  $p(x, t)$  is the time derivative of the velocity potential  $\varphi(x, t)$  (see, for example [10]), so that

$$\begin{aligned} V(x, t) &= \frac{1}{\rho} \nabla \varphi(x, t), \\ p(x, t) &= \frac{\partial}{\partial t} \varphi(x, t). \end{aligned} \quad (12)$$

(Velocity potential  $\varphi(x, t)$  also satisfies the wave equation (11).)

Now, by taking into account (12), equation (10) can be re-written as

$$M(t) = \frac{1}{\rho} B \cdot \int_{\Omega} J_I(x) \times \nabla \varphi(x, t) dx.$$

Further, by noticing that  $\nabla \times (\varphi J_I) = -J_I \times \nabla \varphi + \varphi \nabla \times J_I$  we obtain

$$\begin{aligned} M(t) &= \frac{1}{\rho} B \cdot \left[ - \int_{\Omega} \nabla \times (\varphi J_I) dx + \int_{\Omega} \varphi(x, t) \nabla \times J_I(x) dx \right] \\ &= \frac{1}{\rho} B \cdot \left[ \int_{\partial\Omega} \varphi(z, t) J_I(z) \times n(z) dA(z) + \int_{\Omega} \varphi(x, t) \nabla \times J_I(x) dx \right]. \end{aligned} \quad (13)$$

In some situations the above equations can be further simplified. For example, if at some moment of time  $t$  velocity potential  $\varphi(x, t)$  vanishes on the boundary  $\partial\Omega$ , then the surface integral in (13) also vanishes:

$$M(t) = \frac{1}{\rho} B \cdot \int_{\Omega} \varphi(x, t) \nabla \times J_I(x) dx. \quad (14)$$

Similarly, if boundary  $\partial\Omega$  is located far away from the support of inhomogeneity of  $\sigma(x)$ , the surface integral in (13) can be neglected, and we again obtain equation (14).

Equation (13) is our mathematical model of the MAET measurements. Our goal is to reconstruct from the data  $M(t)$  conductivity  $\sigma(x)$  — by varying  $B$ ,  $\varphi(x, t)$ , and  $I(z)$ . Our strategy for solving this problem is outlined in the following sections. However, some conclusions can be reached just by looking at the equation (13). For example, one can notice that if three sets of measurements are conducted with magnetic induction pointing respectively in the directions of canonical basis vectors  $e_1$ ,  $e_2$ , and  $e_3$ , one can easily reconstruct the sum of integrals in the brackets in (13). Further, if one focuses  $\varphi(x, t)$  so that at the moment  $t = 0$  it becomes the Dirac  $\delta$ -function centered at  $y$ , i.e.

$$\varphi(x, 0) = \delta(x - y)$$

then one immediately obtains the value of  $\nabla \times J_I$  at the point  $y$  (such a focusing is theoretically possible as explained in the next section). Thus, by moving the focusing point through the object, one can reconstruct the curl of  $J_I$  in all of  $\Omega$ .

Our model also explains the observation reported in [13] that no signal is obtained when the acoustic wavepacket is passing through the regions of constant  $\sigma(x)$ . In such regions current field  $J_I$  is irrotational and, therefore, the integral in (14) vanishes.

Finally, it becomes clear that an accurate image reconstruction is impossible if monochromatic acoustic waves of only a single frequency  $k$  are used for scanning, no matter how well they are focused. In this case the spatial component  $\psi$  of  $\varphi(x, t) = \psi(x) \exp(ikt)$  is a solution of the Helmholtz equation

$$\Delta\psi + k^2\psi = 0,$$

and can be approximated in  $\Omega$  by the plane waves  $e^{i\lambda \cdot x}$  with  $|\lambda| = k$ . Let us assume for simplicity that the electrical boundary is removed to infinity. Then, measuring data  $M(t)$  given by (14) is equivalent to collecting values of the Fourier transform of  $\nabla \times J_I(x)$  corresponding to the wave vectors  $\lambda$  lying on the sphere  $|\lambda| = k$  in the Fourier domain. All the other spatial frequencies cannot be recovered.

## 2. Reconstructing the curls of currents

The first step toward solving the inverse problem of MAET is reconstruction of the curls of currents  $J_I(x)$  corresponding to certain choices of  $I(z)$ . Let us assume that all the measurements are repeated three times, with magnetic induction  $B$  pointing respectively in the directions of canonical basis vectors  $e_1$ ,  $e_2$ , and  $e_3$ . Then, as mentioned above, if  $\varphi(x, 0) = \delta(x - y)$ , one readily recovers from the data  $M(0)$  the curl of the current at  $y$ , i.e.  $\nabla \times J_I(y)$ . Generating such a velocity potential is possible at least theoretically. For example, if one simultaneously propagates plane waves  $\varphi_\lambda(x, t) = \exp(i\lambda \cdot x - i|\lambda|t)$  with all possible wave vectors  $\lambda$ , the combined velocity potential at the moment  $t = 0$  will add up to the Dirac delta-function  $\delta(x)$ . Such an arrangement is rather impractical: firstly, the sources of sound would have to be removed far from the object to produce a good approximation to plane waves within the object. Secondly, they would have to completely surround the object, and, finally, all the sources would have to be synchronized. A variation of this approach is to place small point-like sources in the vicinity of the object. Then instead of plane waves, propagating spherical fronts (or monochromatic waves) would be generated. These types of waves can also be focused into a delta-function (a discussion of such focusing can be found in [19]).

### 2.1. Synthetic focusing

However, a more practical approach is to utilize some realistic measuring configuration (e.g. one consisting of one or several small sources scanning the boundary sequentially), and then to synthesize algorithmically from the realistic data the desired measurements that correspond to the delta-like velocity potential. Such a *synthetic focusing* was first introduced in the context of hybrid methods in [18, 19, 24]. It was shown, in applications to AET and to the acoustically modulated optical tomography, that synthetic focusing is equivalent to solving the inverse problem of TAT. The latter problem has been studied extensively, and a wide variety of methods is known by now (see reviews [17, 33] and references therein). The same technique can be applied to MAET, as explained below.

*2.1.1. Measuring functionals solve the wave equation* Consider a propagating spherical front originated at the point  $y$ . If the initial conditions on  $p_y(x, t)$  are

$$\begin{cases} p_y(x, 0) = \delta(x - y), \\ \frac{\partial}{\partial t} p_y(x, 0) = 0, \end{cases}$$

then  $p_y(x, t)$  can be represented in the whole of  $\mathbb{R}^3$  by means of the Kirchhoff formula [32]

$$p_y(x, t) = \frac{\partial}{\partial t} \frac{\delta(|x - y| - ct)}{4\pi|x - y|}.$$

Such a front can be generated by a small transducer placed at  $y$  and excited by a delta-like electric pulse; such devices are common in ultrasonic imaging.

Velocity potential  $\varphi(x, y, t)$  corresponding to  $p_y(x, t)$  then equals

$$\varphi(x, y, t) = \frac{\delta(|x - y| - ct)}{4\pi|x - y|}. \quad (15)$$

The role of variables  $x$  and  $y$  is clearly interchangeable;  $\varphi(x, y, t)$  is the retarded Green's function of the wave equation [32] either in  $x$  and  $t$ , or in  $y$  and  $t$ . Moreover, consider the following convolution  $H(y, t)$  of a finitely supported smooth function  $h(y)$  with  $\varphi$

$$H(y, t) = \int_{\mathbb{R}^3} h(y) \frac{\delta(|x - y| - ct)}{4\pi|x - y|} dx.$$

Then  $H(y, t)$  is the solution of the following initial value problem (IVP) in  $\mathbb{R}^3$  [32]:

$$\begin{cases} \frac{1}{c^2} \frac{\partial^2}{\partial t^2} H(y, t) = \Delta_y H(y, t) \\ H(y, 0) = 0, \\ \frac{\partial}{\partial t} H(y, 0) = h(y). \end{cases} \quad (16)$$

Suppose now that a set of MAET measurements is obtained with propagating wave fronts  $\varphi(x, y, t)$  with different centers  $y$  (while  $I(z)$  and  $B$  are kept fixed). By substituting (15) into (13) we find that, for each  $y$ , the corresponding measuring functional  $M_{I,B}(y, t)$  can be represented as the sum of two terms:

$$M_{I,B}(y, t) = M_{I,B}^{\text{sing}}(y, t) + M_{I,B}^{\text{reg}}(y, t),$$

where

$$M_{I,B}^{\text{sing}}(y, t) = \frac{1}{\rho} \int_{\partial\Omega} \frac{\delta(|z - y| - ct)}{4\pi|z - y|} B \cdot J_I(z) \times n(z) dA(z), \quad (17)$$

$$M_{I,B}^{\text{reg}}(y, t) = \frac{1}{\rho} \int_{\Omega} \frac{\delta(|x - y| - ct)}{4\pi|x - y|} B \cdot \nabla \times J_I(x) dx. \quad (18)$$

It is clear from the above discussion that both terms  $M_{I,B}^{\text{sing}}(y, t)$  and  $M_{I,B}^{\text{reg}}(y, t)$  solve the wave equation in  $\mathbb{R}^3$ , subject to the initial conditions

$$\frac{\partial}{\partial t} M_{I,B}^{\text{sing}}(x, 0) = \frac{1}{\rho} B \cdot J_I(x) \times n(x) \delta_{\partial\Omega}(x), \quad (19)$$

$$\frac{\partial}{\partial t} M_{I,B}^{\text{reg}}(x, 0) = \frac{1}{\rho} B \cdot \nabla \times J_I(x), \quad (20)$$

$$M_{I,B}^{\text{sing}}(y, 0) = M_{I,B}^{\text{reg}}(y, 0) = 0, \quad (21)$$

where  $\delta_{\partial\Omega}(x)$  is the delta-function supported on  $\partial\Omega$ . While singular term  $M_{I,B}^{\text{sing}}(y, t)$  solves the wave equation in the sense of distributions, the regular term  $M_{I,B}^{\text{reg}}(y, t)$  represents a classical solution of the wave equation.

**Proposition 1** *Suppose conductivity  $\sigma(x)$  and boundary currents  $I(z)$  are  $C^\infty$  functions of their arguments, and the boundary  $\partial\Omega$  is infinitely smooth. Then the regular part  $M_{I,B}^{\text{reg}}(y, t)$  of the measuring functional is a  $C^\infty$  solution of the wave equation*

$$\frac{1}{c^2} \frac{\partial^2}{\partial t^2} M_{I,B}^{\text{reg}}(y, t) = \Delta_y M_{I,B}^{\text{reg}}(y, t), \quad y \in \mathbb{R}^3, \quad t \in [0, \infty), \quad (22)$$

satisfying initial conditions (20) and (21).

**Proof.** Under the above conditions, potential  $w_I(x)$  solving the boundary value problem (5), (6) is a  $C^\infty$  function in  $\Omega$  due to the classical estimates on the smoothness of solutions of elliptic equations with smooth coefficients [12]. The curl of  $J_I$  vanishes outside of  $\Omega_1$  since  $\sigma(x)$  is constant in  $\Omega \setminus \Omega_1$ . Therefore, the right hand side of (20) can be extended by zero to a  $C^\infty$  function in  $\mathbb{R}^3$ . Term  $M_{I,B}^{\text{reg}}(y, t)$  defined by equation (18) solves wave equation (22) (due to the Kirchhoff formula [32]) subject to infinitely smooth initial conditions (20), (21), and thus it is a  $C^\infty$  function for all  $y \in \mathbb{R}^3, t \in [0, \infty)$ . ■

*2.1.2. Reconstructing the initial conditions* We would like to reconstruct the right hand side of (20) (and, possibly that of (19)) from the measured values of  $M_{I,B}(y, t)$ . Since  $c$  is assumed constant, in the 3D case  $M_{I,B}(y, t)$  will vanish (due to the Huygens principle) for  $t > t_{\max} = D_{\max}/c$  where  $D_{\max}$  is the maximal distance between the points of  $\Omega$  and the acoustic sources. We will assume that  $M_{I,B}(y, t)$  is measured for all  $t \in [0, t_{\max}]$ .

The problem of reconstructing  $\frac{\partial}{\partial t} M_{I,B}(x, 0)$  from  $M_{I,B}(y, t)$  is equivalent to that of reconstructing the initial value  $h(y)$  from the solution of IVP (16). The latter, more general problem, has been studied extensively in the context of TAT (see, e.g. [17, 33] and references therein). In the case of TAT, points  $y$  describe the location of detectors rather than sources, but the rest of the mathematics remains the same. The most studied situation is when the detectors are placed on a closed surface  $\Sigma$  surrounding the object. If  $\Sigma$  is a sphere, a variety of inversion techniques is known, including (but not limited to) the explicit inversion formulae [11, 20, 28], series techniques [21, 23, 27, 35], time reversal by means of finite differences [2, 7, 14], etc. If  $\Sigma$  is a surface of a cube, one can use the inversion formula [22], the already mentioned time reversal methods, or the fast algorithm developed in [21] for such surfaces.

The choice of the TAT inversion method for application in MAET will depend, in particular, on the mutual location of the electric boundary  $\partial\Omega$  and the acoustic source surface  $\Sigma$ . One can decide to move the electric boundary further away by placing the object in a liquid with conductivity equal to 1 and by submerging the acoustic sources into the liquid, in which case  $\Sigma$  will be inside  $\partial\Omega$ . Alternatively, one can move the acoustic surface further away so that it surrounds the electric boundary. And, finally,



one may choose to conduct the electrical measurements on the surface of the body, and to place the acoustic sources on the same surface, in which case  $\Sigma$  will coincide with  $\partial\Omega$ .

If  $\partial\Omega$  lies inside  $\Sigma$ , all the above mentioned TAT inversion techniques (theoretically) will reconstruct both  $\frac{\partial}{\partial t}M_{I,B}^{\text{sing}}(y, 0)$  and  $\frac{\partial}{\partial t}M_{I,B}^{\text{reg}}(y, 0)$ . In practice, accurate numerical reconstruction of the singular term  $\frac{\partial}{\partial t}M_{I,B}^{\text{sing}}(y, 0)$  supported on  $\partial\Omega$  may be difficult to obtain due to the finite resolution of any realistic measurement system. Luckily, the support  $\Omega_1$  of  $\frac{\partial}{\partial t}M_{I,B}^{\text{reg}}(y, 0)$  (i.e. ) is spatially separated from  $\partial\Omega$ , so that the contributions from the singular term can be eliminated just by setting the reconstructed image to zero outside  $\Omega_1$ . As explained further in the paper,  $\frac{\partial}{\partial t}M_{I,B}^{\text{reg}}(y, 0)$  contains enough information to reconstruct the conductivity. On the other hand,  $\frac{\partial}{\partial t}M_{I,B}^{\text{sing}}(y, 0)$  does carry some useful information, which can be recovered by a specialized reconstruction algorithm.

If  $\Sigma$  lies inside  $\partial\Omega$  (but  $\Omega_1$  still lies inside  $\Sigma$ ), not all TAT reconstruction techniques can be applied. Most inversion formulae will produce an incorrect result in the presence of the exterior sources (such as the term  $\frac{\partial}{\partial t}M_{I,B}^{\text{sing}}(y, 0)$  supported on  $\partial\Omega$  and exterior with respect to the region enclosed by  $\Sigma$ ). On the other hand, formula [22], series methods [21] and all the time reversal techniques automatically filter out the exterior sources and thus can be used to reconstruct  $\frac{\partial}{\partial t}M_{I,B}^{\text{reg}}(y, 0)$ .

The situation is more complicated if surfaces  $\Sigma$  and  $\partial\Omega$  coincide. However, those methods that are insensitive to sources located outside  $\partial\Omega$  are also insensitive to the sources located on  $\partial\Omega$ , particularly to those represented by  $\frac{\partial}{\partial t}M_{I,B}^{\text{sing}}(y, 0)$ . These methods can be used to reconstruct  $\frac{\partial}{\partial t}M_{I,B}^{\text{reg}}(y, 0)$ . In other words, the following proposition holds:

**Proposition 2** *If values of measuring functional  $M_{I,B}(y, t)$  are known for all  $y \in \Sigma$  and  $t \in [0, D_{\max}/c]$ , the term  $\frac{\partial}{\partial t}M_{I,B}^{\text{reg}}(y, 0)$  can be exactly reconstructed in  $\Omega_1$  (by using one of the above-mentioned TAT algorithms). Moreover, if the conditions of Proposition 1 are satisfied, the reconstruction is exact point-wise.*

In order to reconstruct the curl of the current  $J_I(x)$ , we need to repeat the procedure of finding  $\frac{\partial}{\partial t}M_{I,B}^{\text{reg}}(x, 0)$  three times, with three different orientations of  $B$ :  $B^{(j)} = |B|e_j$ ,  $j = 1, 2, 3$ . As a result, we find the projections of  $\nabla \times J_I(x)$  on all  $e_j$ 's, and thus obtain:

$$\nabla \times J_I(x) = \frac{\rho}{|B|} \sum_{j=1}^3 e_j \frac{\partial}{\partial t} M_{I,B^{(j)}}^{\text{reg}}(x, 0), \quad x \in \Omega_1. \quad (23)$$

(outside  $\Omega_1$  the curl of  $J_I(x)$  equals 0 since  $\sigma(x)$  is constant in  $\Omega \setminus \Omega_1$ ).

If, in addition,  $\partial\Omega$  lies inside  $\Sigma$  and  $\frac{\partial}{\partial t}M_{I,B}^{\text{sing}}(y, 0)$  has been recovered, we also obtain

$$J_I(x) \times n(x) \delta_{\partial\Omega}(x) = \frac{\rho}{|B|} \sum_{j=1}^3 e_j \frac{\partial}{\partial t} M_{I,B^{(j)}}^{\text{sing}}(x, 0). \quad (24)$$

### 3. Reconstructing currents from the curls

The considerations of the previous section show how to recover from the values of the measuring functionals  $M_{I,B^{(j)}}(y, t)$  the curl of  $J_I$  and, in some situations, the surface term (24). The next step is to reconstruct current  $J_I$  itself.

We know that  $J_I$  satisfies the following boundary conditions:

$$J_I \cdot n|_{\partial\Omega} = \frac{\partial}{\partial n} w_I \Big|_{\partial\Omega} = I. \quad (25)$$

In certain simple domains one can find a way to solve the equation

$$C = \nabla \times J_I$$

for  $J_I$  in such a way that conditions (25) are satisfied automatically. One such domain is a cube; we present the corresponding algorithm in Section 5. In general, however, solution of an auxiliary Neumann problem may be needed as discussed below.

Let us start with the most general situation and assume that only the curl  $C = \nabla \times J_I$  has been reconstructed. Since current  $J_I$  is a purely solenoidal field whose curl vanishes on  $\partial\Omega$ , there exists a vector potential  $K(x)$  such that

$$J_I(x) = \nabla \times K(x) + \Psi(x), \quad x \in \Omega, \quad (26)$$

where  $K(x)$  has the form

$$K(x) = \int_{\Omega} \frac{C(y)}{4\pi|x-y|} dy,$$

and  $\Psi(x)$  is both a solenoidal and potential field within  $\Omega$ . Then there exists harmonic potential  $\psi(x)$  such that  $\Psi(x) = \nabla\psi(x)$ . Therefore, by combining equations (26) and (25) one obtains

$$\left( n \cdot (\nabla \times K)(z) + \frac{\partial}{\partial n} \psi(z) \right) \Big|_{\partial\Omega} = I(z),$$

and  $\psi(z)$  now can be recovered by solving the Neumann problem

$$\begin{cases} \Delta\psi(x) = 0, & x \in \Omega \\ \frac{\partial}{\partial n} \psi(z) = I(z) - n \cdot \left( \nabla \times \int_{\Omega} \frac{C(y)}{4\pi|z-y|} dy \right), & z \in \partial\Omega. \end{cases} \quad (27)$$

Now  $J_I(x)$  is uniquely defined by the formula

$$J_I(x) = \nabla \times \int_{\Omega} \frac{C(y)}{4\pi|x-y|} dy + \nabla\psi(x), \quad x \in \Omega. \quad (28)$$

**Proposition 3** *Under smoothness assumptions of Proposition 1, current  $J_I(x)$  is given by (28), where function  $\psi(x)$  is the (classical) solution of the Neumann problem (27).*

If, in addition to the curl  $\nabla \times J_I(x)$ , the surface term (equation (24)) has been reconstructed, there is no need to solve the Neumann problem. Instead, function  $\Psi(x)$  is given explicitly by the following formula [31]:

$$\Psi(x) = \nabla_x \times \int_{\partial\Omega} \frac{J_I(y) \times n(y)}{4\pi|x-y|} dA(y).$$

The final expression for current  $J_I$  can now be written as

$$\begin{aligned} J_I(x) &= \nabla_x \times \left[ \int_{\Omega} \frac{C(y)}{4\pi|x-y|} dy + \int_{\partial\Omega} \frac{J_I(y) \times n(y)}{4\pi|x-y|} dA(y) \right] \\ &= \nabla_x \times \int_{\bar{\Omega}} \frac{C(y) + J_I(y) \times n(y) \delta_{\partial\Omega}(y)}{4\pi|x-y|} dy, \quad x \in \Omega, \end{aligned} \quad (29)$$

where  $\bar{\Omega}$  is the closure  $\Omega$ . The term with the delta-function in the numerator of (29) coincides with the surface term (24). In order to avoid the direct numerical reconstruction of the singular term, one may want to try to modify the utilized TAT reconstruction algorithm so as to recover directly the convolution with  $\frac{1}{4\pi|x|}$  contained in equation (29). The practicality of such an approach requires further investigation.

#### 4. Reconstructing conductivity from the currents

In order to reconstruct  $\sigma(x)$  we utilize three currents  $J^{(k)}$ ,  $k = 1, 2, 3$ , corresponding to different boundary conditions  $I_k$ . We are also using three different magnetic inductions  $B^{(j)}$ ,  $j = 1, 2, 3$ , and, as a result, obtain the values of the following measuring functionals:

$$M_{I_k, B^{(j)}}(y, t) = \int_{\partial\Omega} I_k(z) u_{(j)}(z, t) dA(z), \quad j = 1, 2, 3, \quad k = 1, 2, 3, \quad (30)$$

where  $u_{(j)}(z, t)$  is the electric potential corresponding to the acoustic wave with the velocity potential  $\varphi(x, z, t)$  propagating through the body in the presence of constant magnetic field  $B^{(j)}$ . The increase in the number of currents  $J^{(k)}$  does not require additional physical measurements: the same measured boundary values of  $u_{(j)}(z, t)$  are used to compute different functionals by changing the integration weight  $I_k(z)$  in (4).

For each of the currents  $J^{(k)}$  we apply one of the above-mentioned TAT reconstruction techniques to compute  $\frac{\partial}{\partial t} M_{I_k, B^{(j)}}(y, 0)$ . The knowledge of the latter functions for  $B^{(j)}$ ,  $j = 1, 2, 3$ , allows us to recover the curls  $C^{(k)} = \nabla \times J^{(k)}$ ,  $k = 1, 2, 3$ , (equation (23)) and, possibly, the surface terms (24). Finally, currents  $J^{(k)}$  are reconstructed by one of the methods described in the previous section.

At the first sight, finding  $\sigma(x)$  from the knowledge of  $J^{(k)} = \sigma \nabla w_{I_k}$ ,  $k = 1, 2, 3$ , is a non-linear problem, since the unknown electric potentials  $w_{I_k}$  depend on  $\sigma(x)$ . However, as shown below, this problem can be solved explicitly without a linearization or some other approximation. Indeed, for any  $k = 1, 2, 3$ , the following formula holds:

$$0 = \nabla \times \frac{J^{(k)}}{\sigma} = \left( \nabla \frac{1}{\sigma} \right) \times J^{(k)} + \frac{1}{\sigma} C^{(k)} = -\frac{1}{\sigma^2} (\nabla \sigma) \times J^{(k)} + \frac{1}{\sigma} C^{(k)}$$

so that

$$\nabla \ln \sigma(x) \times J^{(k)}(x) = C^{(k)}(x), \quad x \in \Omega, \quad k = 1, 2, 3. \quad (31)$$

Now one can try to find  $\nabla \ln \sigma$  at each point in  $\Omega$  by solving the (in general) over-determined system of linear equations (31).

Let us assume first, that at each point  $x$  in  $\Omega$  currents  $J^{(l)}(x)$ ,  $l = 1, 2, 3$  form a basis in  $\mathbb{R}^3$ . There are 9 equations in system (31), whose unknowns are the three components of  $\nabla \ln \sigma$ , but the rank of the corresponding matrix does not exceed 6. In order to see this, let us multiply each equation of (31) by  $J^{(l)}$ ,  $l = 1, 2, 3$ . (Since currents  $J^{(l)}$  form a basis, this is equivalent to a multiplication by a non-singular matrix). We obtain

$$\begin{cases} \nabla \ln \sigma \cdot (J^{(1)} \times J^{(2)}) = C^{(1)} \cdot J^{(2)} \\ \nabla \ln \sigma \cdot (J^{(1)} \times J^{(2)}) = -C^{(2)} \cdot J^{(1)} \\ \nabla \ln \sigma \cdot (J^{(1)} \times J^{(3)}) = C^{(1)} \cdot J^{(3)} \\ \nabla \ln \sigma \cdot (J^{(1)} \times J^{(3)}) = -C^{(3)} \cdot J^{(1)} \\ \nabla \ln \sigma \cdot (J^{(2)} \times J^{(3)}) = C^{(2)} \cdot J^{(3)} \\ \nabla \ln \sigma \cdot (J^{(2)} \times J^{(3)}) = -C^{(3)} \cdot J^{(2)} \end{cases}.$$

In the absence of noise the right hand sides of equations number 2, 4, and 6 in the above system would coincide with those of equations 1, 3, and 5, respectively, and therefore three equations could be dropped from the system. However, in order to reduce the noise sensitivity of the method, we average the equations with identical left sides (this is equivalent to finding the least squares solution of this system). We thus obtain:

$$\begin{cases} \nabla \ln \sigma \cdot (J^{(1)} \times J^{(2)}) = R_1, & R_1 = \frac{1}{2}(C^{(1)} \cdot J^{(2)} - C^{(2)} \cdot J^{(1)}), \\ \nabla \ln \sigma \cdot (J^{(1)} \times J^{(3)}) = R_2, & R_2 = \frac{1}{2}(C^{(1)} \cdot J^{(3)} - C^{(3)} \cdot J^{(1)}), \\ \nabla \ln \sigma \cdot (J^{(2)} \times J^{(3)}) = R_3, & R_3 = \frac{1}{2}(C^{(2)} \cdot J^{(3)} - C^{(3)} \cdot J^{(2)}). \end{cases} \quad (32)$$

As shown in Appendix, the solution of (32) can be written explicitly as follows:

$$\nabla \ln \sigma = \frac{1}{J^{(1)} \cdot (J^{(2)} \times J^{(3)})} A \mathbf{R}, \quad (33)$$

where  $\mathbf{R} = (R_3, -R_2, R_1)^T$ , and  $A$  is  $(3 \times 3)$  matrix whose columns are the Cartesian coordinates of the currents  $J^{(1)}$ ,  $J^{(2)}$ , and  $J^{(3)}$ , respectively. Since, by assumption, currents  $J^{(l)}$  form a basis at each point of  $\Omega$ , the denominator in (33) never vanishes and, thus, equation (33) can be used to reconstruct  $\nabla \ln \sigma$  in all of  $\Omega$ .

Finally, we compute the divergence of both sides in (33):

$$\Delta \ln \sigma = \nabla \cdot \frac{A \mathbf{R}}{J^{(1)} \cdot (J^{(2)} \times J^{(3)})}, \quad (34)$$

and solve Poisson equation (34) for  $\ln \sigma$  in  $\Omega$  subject to the Dirichlet boundary conditions

$$\ln \sigma|_{\partial\Omega} = 0. \quad (35)$$

The above reconstruction procedure works if currents  $J^{(k)}(x)$   $k = 1, 2, 3$ , are linearly independent at each  $x \in \Omega$ . In general, this cannot be guaranteed. There exists a counterexample [8] with such a conductivity and a boundary condition that the corresponding current vanishes at a point within the domain. Such a situation, however, is unlikely to occur for a realistic  $\sigma(x)$ , and our method should still be useful.

Moreover, the condition of three currents forming a basis at each  $x \in \Omega$  can be relaxed. Let us show that if one of the currents (say,  $J^{(3)}$ ) vanishes at some  $x$  and the two other currents are not parallel in  $x$  the following system is still uniquely solvable:

$$\begin{cases} \nabla \ln \sigma \times J^{(1)} = C^{(1)} \\ \nabla \ln \sigma \times J^{(2)} = C^{(2)} \end{cases} \quad (36)$$

Indeed, let us multiply via dot product the above equations by  $J^{(2)}$  and  $J^{(1)}$  respectively, and subtract them. We obtain

$$\nabla \ln \sigma \cdot (J^{(1)} \times J^{(2)}) = \frac{1}{2} (C^{(1)} \cdot J^{(2)} - C^{(2)} \cdot J^{(1)}). \quad (37)$$

Now, multiply the first equation in (36) by  $J^{(1)} \times J^{(2)}$ . The left hand side yields

$$\begin{aligned} (\nabla \ln \sigma \times J^{(1)}) \cdot (J^{(1)} \times J^{(2)}) &= \nabla \ln \sigma \cdot [J^{(1)} \times (J^{(1)} \times J^{(2)})] \\ &= \nabla \ln \sigma \cdot [(J^{(1)} \cdot J^{(2)}) J^{(1)} - (J^{(1)} \cdot J^{(1)}) J^{(2)}], \end{aligned}$$

which leads to the equation

$$\nabla \ln \sigma \cdot [(J^{(1)} \cdot J^{(2)}) J^{(1)} - (J^{(1)} \cdot J^{(1)}) J^{(2)}] = C^{(1)} \cdot (J^{(1)} \times J^{(2)}). \quad (38)$$

Similarly, by multiplying the second equation in (36) by  $(J^{(2)} \times J^{(1)})$  we obtain

$$\nabla \ln \sigma \cdot [(J^{(1)} \cdot J^{(2)}) J^{(2)} - (J^{(2)} \cdot J^{(2)}) J^{(1)}] = C^{(2)} \cdot (J^{(2)} \times J^{(1)}). \quad (39)$$

Equations (37), (38) and (39) form a linear system with three equations and three unknowns. This system is solvable since the vectors given by the bracketed expressions in (38) and (39) are not parallel. Indeed, the cross-product of these terms yields

$$[\dots] \times [\dots] = (J^{(1)} \times J^{(2)}) \left[ (J^{(1)} \cdot J^{(2)})^2 - (J^{(1)} \cdot J^{(1)}) (J^{(2)} \cdot J^{(2)}) \right].$$

The above expression is clearly non-zero if  $J^{(1)}$  and  $J^{(2)}$  are not parallel, and therefore the system of the three equations (37), (38), (39) is uniquely solvable in this case.

**Theorem 4** *Suppose that the conditions of Proposition 1 are satisfied, and that the conductivity  $\sigma(x)$  and boundary currents  $I_k$ ,  $k = 1, 2, 3$ , are such that at each point  $x \in \Omega$  two of the three correspondent currents  $J^{(k)}$  are non-parallel. Then the logarithm of the conductivity  $\ln \sigma$  is uniquely determined by the values of the measuring functionals  $M_{I_k, B^{(j)}}(y, t)$ ,  $k = 1, 2, 3$ ,  $j = 1, 2, 3$ ,  $y \in \Sigma$  and  $t \in [0, D_{\max}/c]$ .*

**Proof.** By Propositions 1, 2, 3, and 4, from the values of  $M_{I_k, B^{(j)}}(y, t)$  one can reconstruct currents  $J^{(k)}(x)$ ,  $k = 1, 2, 3$ , at each  $x \in \Omega$ . Since at each  $x$  at least two of the three currents (lets call them  $J^{(1)}$ , and  $J^{(2)}$ ) are not parallel, system of the three equations (37), (38), (39) is uniquely solvable, and  $\nabla \ln \sigma$  can be found at each  $x \in \Omega$ . Since  $\sigma$  is bounded away from zero,  $\nabla \ln \sigma$  is a  $C^\infty$  function in  $\Omega$ . By computing the

divergence of  $\nabla \ln \sigma$  the problem of finding  $\ln \sigma$  reduces to solving the Poisson problem with zero Dirichlet boundary conditions in a smooth domain  $\Omega$ . ■

The condition that out of the three currents two are non-zero and not parallel, is less restrictive than the requirement that the three currents are linearly independent. To the best of our knowledge, there exists no counterexample showing that the former condition can be violated, i.e. that one of the three currents generated by linearly independent boundary conditions vanishes and the other two are parallel at some point in space. On the other hand, we know of no proof that this cannot happen.

## 5. The case of a rectangular domain

In the previous sections we presented a theoretical scheme for finding the currents  $J^{(k)}$ ,  $k = 1, 2, 3$ , and conductivity  $\sigma(x)$  from the MAET measurements in a rather general setting, where the electrical domain  $\Omega$  and surface  $\Sigma$  supporting the acoustic sources were quite arbitrary. This scheme consists in solving the inverse problem of TAT in the domain surrounded by  $\Sigma$ , the Neumann problem for the Laplace equation in  $\Omega$ , and the Poisson equation for  $\ln \sigma$ , also in  $\Omega$ . All these problems are well-studied and algorithms for their solution are well known. However, in the case when  $\Omega$  is a cube and  $\Sigma$  coincides with  $\partial\Omega$ , the reconstruction can be obtained in the form of an explicit series solution.

### 5.1. Fast reconstruction algorithm

Let us assume that the domain  $\Omega$  is a cube  $[0,1] \times [0,1] \times [0,1]$ , and the sound sources are located on  $\partial\Omega$ . (In practice such a configuration will occur if the object is placed in a cubic tank filled with conductive liquid, with the sources of sound and electrodes placed on the tank walls). We will use three boundary conditions  $I_k$  defined by the formulae:

$$I_k(x) = \begin{cases} \frac{1}{2}, & x \in \partial\Omega, \quad x_k = 1 \\ -\frac{1}{2}, & x \in \partial\Omega, \quad x_k = 0 \\ 0, & x \in \partial\Omega, \quad 0 < x_k < 1 \end{cases}, \quad k = 1, 2, 3, \quad x = (x_1, x_2, x_3). \quad (40)$$

As before, all the measurements are repeated with three different directions of the magnetic field  $B^{(j)} = |B|e_j$ ,  $j = 1, 2, 3$ , and functionals  $M_{I_k, B^{(j)}}(y, t)$  (see equation (30)) are computed from the values of the electrical potentials  $u^{(j)}(x, t)$  on  $\partial\Omega$ , for  $t \in \left[0, \frac{\sqrt{3}}{c}\right]$ .

We start the reconstruction by applying to  $M_{I_k, B^{(j)}}(y, t)$  the fast cubic-domain TAT algorithm [21] to recover the regular terms  $\frac{\partial}{\partial t} M_{I^{(k)}, B^{(j)}}^{\text{reg}}(x, 0)$ ,  $j = 1, 2, 3$ ,  $k = 1, 2, 3$ . (The algorithm we chose automatically sets to zero the sources corresponding to the surface terms  $\frac{\partial}{\partial t} M_{I^{(k)}, B^{(j)}}^{\text{sing}}(x, 0)$  supported on  $\Sigma$ ). This is done for all three directions of  $B^{(j)}$ , so that we immediately obtain the curls  $C^{(k)}(x) = \nabla \times J^{(k)}(x)$ ,  $k = 1, 2, 3$ ,  $x \in \partial\Omega$ .

Now, since the currents are divergence-free,

$$\nabla \times C^{(k)}(x) = \nabla \times \nabla \times J^{(k)}(x) = -\Delta J^{(k)}(x).$$

The above equations are a set of Poisson problems for the components of  $J^{(k)}$  in  $\Omega$ . Below we discuss how to enforce the correct boundary conditions for these problems.

Let us recall that

$$J^{(k)}(x) = \sigma \nabla w^{(k)}(x),$$

where  $w^{(k)}$  is the corresponding electric potential. It is convenient to subtract the linear component from potentials, i.e. to introduce  $w^{(k),0}(x)$  and  $J^{(k),0}(x)$  defined as follows:

$$\begin{aligned} w^{(k)}(x) &= w^{(k),0}(x) + x_k, \\ J^{(k)}(x) &= J^{(k),0}(x) + e_k, \quad k = 1, 2, 3. \end{aligned}$$

Now each  $w^{(k),0}$  satisfies zero Neumann conditions on  $\partial\Omega$ , and thus can be extended by even reflections to a periodic function in  $\mathbb{R}^3$ . Since  $w^{(k),0}$  is a harmonic function near  $\partial\Omega$ , such an extension will be a harmonic function in the neighborhood of  $\partial\Omega$ . Therefore, each  $w^{(k),0}$  can be expanded in the Fourier cosine series in  $\Omega$ , and the derivatives of this series yield correct behavior of the so-computed  $\nabla w^{(k),0}$  and  $J^{(k),0}$  on  $\partial\Omega$ . ( $J^{(k),0}$  coincide with  $\nabla w^{(k),0}$  in the vicinity of  $\partial\Omega$ ). Therefore, the components of currents  $J^{(k),0}$  should be expanded in the Fourier series whose basis functions are the corresponding derivatives of the cosine series. In other words, the following series yield correct boundary conditions when used as a basis for expanding currents  $J^{(k),0}$ ,  $k = 1, 2, 3$ :

$$\begin{cases} J_1^{(k),0}(x) = \sum_{l=1}^{\infty} \sum_{m=0}^{\infty} \sum_{n=0}^{\infty} A_{l,m,n}^{(k),1} \sin \pi l x_1 \cos \pi m x_2 \cos \pi n x_3 \\ J_2^{(k),0}(x) = \sum_{l=0}^{\infty} \sum_{m=1}^{\infty} \sum_{n=0}^{\infty} A_{l,m,n}^{(k),2} \cos \pi l x_1 \sin \pi m x_2 \cos \pi n x_3, \\ J_3^{(k),0}(x) = \sum_{l=0}^{\infty} \sum_{m=0}^{\infty} \sum_{n=1}^{\infty} A_{l,m,n}^{(k),3} \sin \pi l x_1 \cos \pi m x_2 \sin \pi n x_3 \end{cases} \quad (41)$$

where  $J^{(k),0}(x) = (J_1^{(k),0}(x), J_2^{(k),0}(x), J_3^{(k),0}(x))$ . Now, since  $\nabla \times J^{(k),0}(x) = \nabla \times J^{(k)}(x)$ :

$$\Delta J^{(k),0}(x) = -\nabla \times C^{(k)}(x), \quad k = 1, 2, 3 \quad (42)$$

and, if the Poisson problems (42) are solved for each component of  $J^{(k),0}$  using sine/cosine Fourier series (41), the correct boundary conditions will be attained. The computation is fast if the Fast Fourier sine and cosine transforms (FFST and FFCT) are utilized.

Notice, that before Poisson problems (42) can be solved, the curl of the  $C^{(k)}$  needs to be computed. This is done by expanding  $C^{(k)}$  in the Fourier sine series and by differentiating the series, again using FFST and FFCT. In other words, we numerically differentiate data that may contain noise. However, this does not give rise to instabilities, since this differentiation is immediately followed by an inverse Laplacian (describing solution of the Poisson problem), so that the combined operator is actually smoothing.

Finally, once the currents are reconstructed, we form the right hand side of the system (34) and solve this Poisson problem for  $\ln \sigma(x)$  by using the Fourier sine series which yields the desired boundary conditions (35). Again, FFST and FFCT are utilized here and in the computations of the divergence needed to form equation (34).

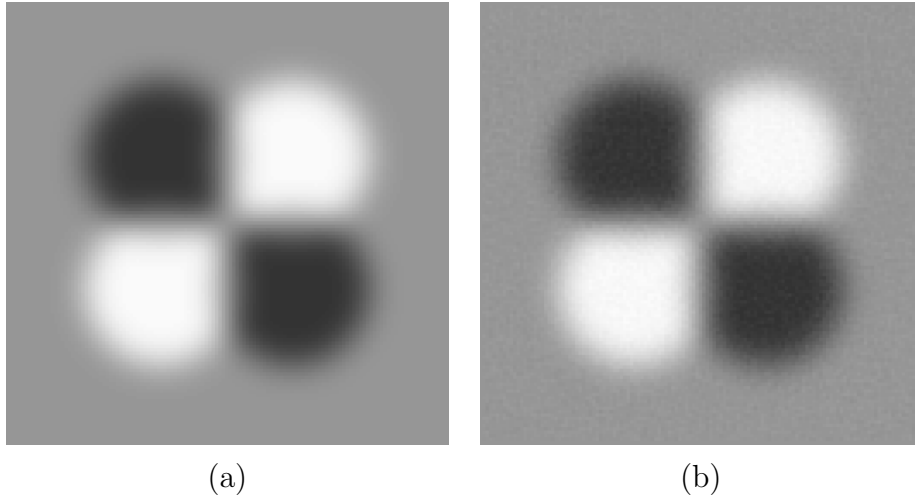


**Figure 1.** A 3D simulation with a smooth phantom representing  $\ln \sigma(x)$   
 (a) the cross section of the phantom by the plane  $x_3 = 0.5$   
 (b) reconstruction from the data with added 50% (in  $L_2$  sense) noise

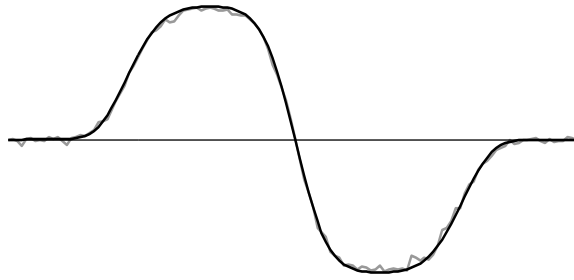


**Figure 2.** The cross section of the reconstructed image (shown in Figure 1) by the line  $x_1 = 0.25$ ,  $x_3 = 0.5$ . The thick black line represents the phantom, the gray line corresponds to the reconstructed image

All the steps of the present algorithm are explicit, and can be performed fast using FFST and FFCT. The same is true for the TAT reconstruction technique [21] used on the first step, so that the required number of floating point operations (flops) for the whole method is  $O(n^3 \ln n)$  for a Cartesian computational grid with  $n^3$  nodes.

## 5.2. Numerical results

We demonstrate the work of the cubic domain reconstruction algorithm on simulated data. For most thorough simulation we would need to solve equation (2) with the boundary conditions (3) for various propagating fronts  $V(x, t)$  centered at different locations on  $\partial\Omega$ . The number of the modeled data points would need to be similar to the number of unknowns. For a fine grid (say, of the size  $257 \times 257 \times 257$ ) we would have to solve equation (2) several million times. This task is too challenging computationally.

Instead, for a given phantom and for the set of functions  $I^{(k)}$  given by (40) we computed currents  $J^{(k)}$  by solving equation (5) with boundary conditions (6). Next,



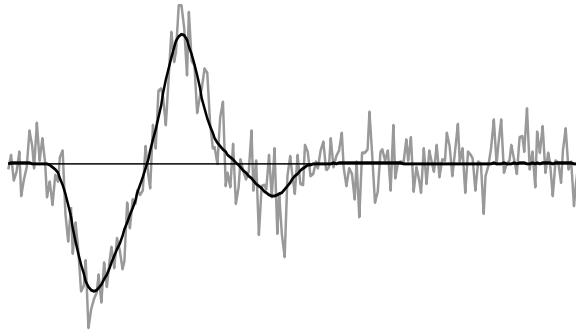


**Figure 3.** Plot of one of the simulated measuring functionals for one of the detector positions (see text for details): thick black line represents accurate values, gray line shows the data with added 50% noise

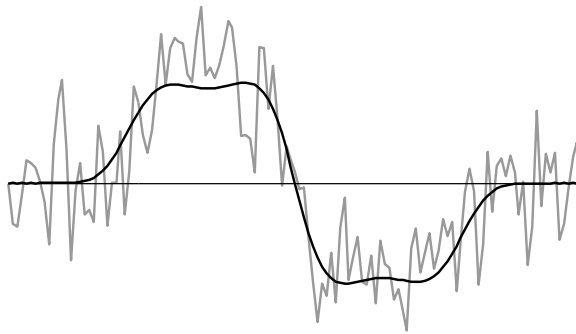


**Figure 4.** Profile of the reconstructed curl (gray line) compared to the accurate values (thick black line). Shown are the values of the third component of  $C^{(1)}$  along the line  $x_2 = 0.5, x_3 = 0.5$

the wave equation (16) with the initial condition  $h(y) = B^{(j)} \cdot \nabla \times J^{(k)}(x)$  was solved for  $j = 1, 2, 3, k = 1, 2, 3$ ; solution of this equation at points in  $\partial\Omega$  simulated the regular part  $\rho M_{I,B}^{\text{reg}}(x, t)$  of the measuring functionals. For simplicity we did not model the singular term  $M_{I,B}^{\text{sing}}(x, t)$  given by (17). Theoretically, when the TAT reconstruction algorithm [21] is applied to such data, this term (not supported in  $\Omega$ ) will not contribute to the reconstruction, and simulating it will not bring additional insight.

As the first phantom simulating  $\ln \sigma(x)$  we used the following linear combinations of four  $C^8$  radially symmetric functions  $\varphi(x - x^{(i)})$ :

$$f(x) = \varphi(|x - x^{(1)}|) - \varphi(|x - x^{(2)}|) - \varphi(|x - x^{(3)}|) + \varphi(|x - x^{(4)}|), \quad (43)$$

where  $\varphi(t)$  is a decreasing non-negative trigonometric polynomial on  $[0, r_0]$ , such that  $\varphi(0) = 0.5$ ,  $\varphi(t) = 0$  for  $t \geq r_0$  and the first eight derivatives of  $\varphi$  vanish at 0 and at  $r_0$ ; centers  $x^{(i)}$  where lying in the plane  $x_3 = 0$ :  $x^{(1)} = (0.25, 0.25, 0)$ ,  $x^{(2)} = (0.25, 0.75, 0)$ ,  $x^{(3)} = (0.75, 0.25, 0)$ ,  $x^{(4)} = (0.75, 0.75, 0)$ . Radius  $r_0$  was equal to 0.34 in this simulation. A gray scale picture of this phantom is shown in Figure 1(a). Figure 1(b) demonstrates the cross-section by the plane  $x_3 = 0.5$  of the image reconstructed on a  $129 \times 129 \times 129$  computational grid from simulated data with added noise. The acoustic sources were

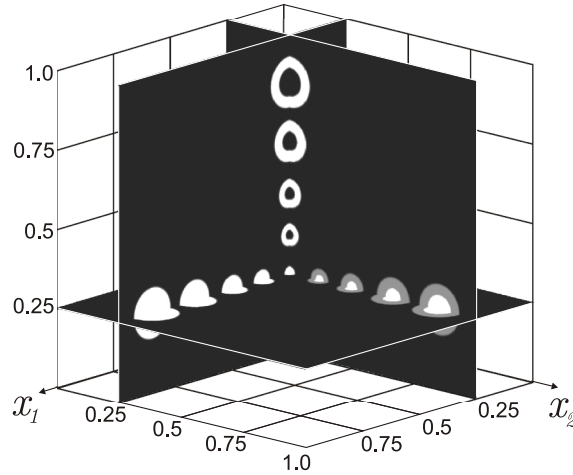


**Figure 5.** The second, (almost) piece-wise constant 3D phantom. Shown are cross sections by the planes  $x_j = 0.25$ ,  $j = 1, 2, 3$

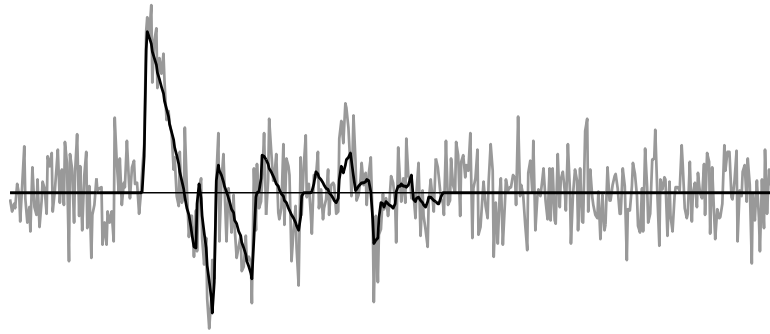


**Figure 6.** Plot of the values of one of the simulated measurement functionals for one of the detector positions (see text for details): thick black line represents accurate values, gray line shows the data with added 100% noise

located at the nodes of  $129 \times 129$  Cartesian grids on each of the six faces of cubic domain  $\Omega$ . For each source 223 values of each measuring functional were computed, representing 223 different time samples (or 223 radii) of the propagating acoustic front.

The measurement noise was simulated by adding values of uniformly distributed random variable to the data. The noise was scaled in such a way that for each time series (one source position) the noise intensity in  $L^2$  norm was 50% of the intensity of the signal (i.e. of the  $L^2$  norm of the data sequence representing the measuring functional). In spite of such high level of noise in the data, the reconstruction shown in Figure 1(b) contains very little noise. This can also be verified by looking at the plot of the cross section of the latter image along the line  $x_2 = 0.25$ , presented in Figure 2.

In order to understand the origins of such unusually low noise sensitivity, we plot in Figure 3 a profile of one of the time series,  $M_{I_1, B^{(3)}}(y, t)$  for point  $y = (1, 0.5, 0.5)$ . The thick black line represents the accurate measurements, the gray line shows the data with

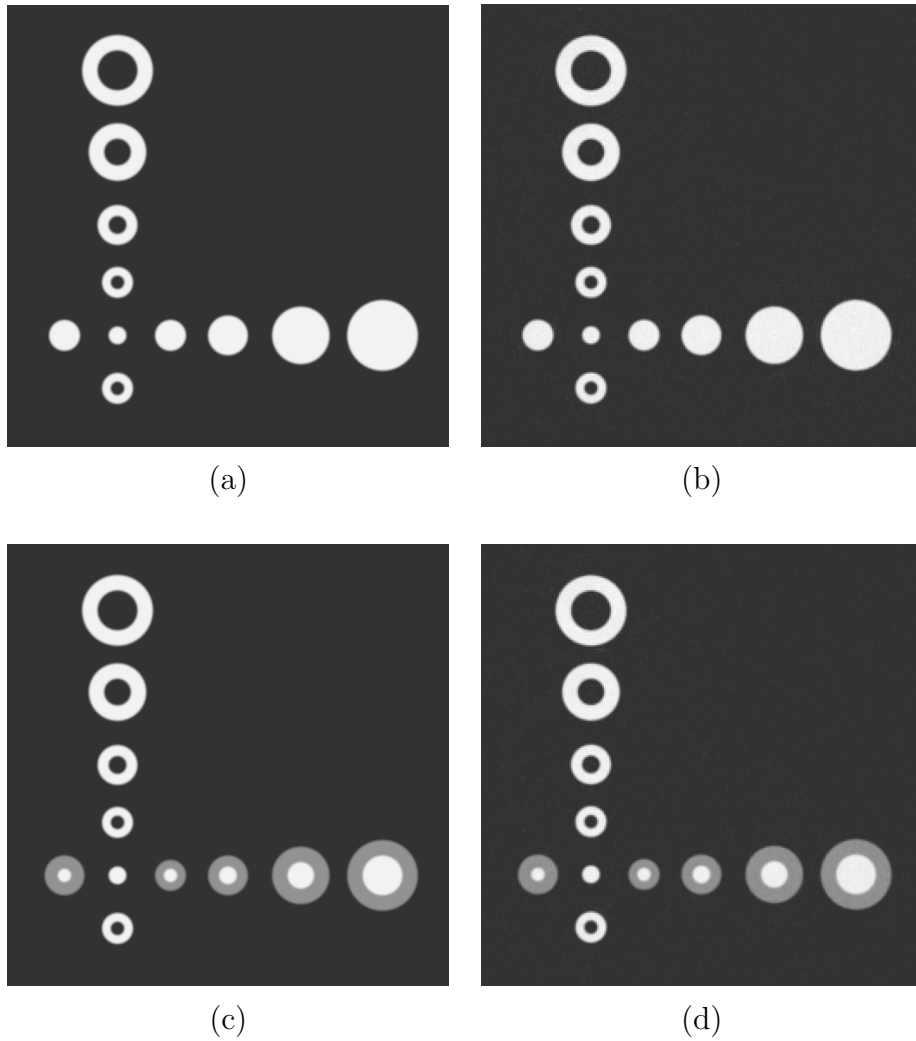


**Figure 7.** Simulation in 3D with phantom shown in Figure 5; (a) and (c) are the cross sections of the phantom by planes  $x_2 = 0.25$  and  $x_1 = 0.25$ , respectively; (b) and (d) are the corresponding cross sections of the reconstruction from the data with added 100% (in  $L_2$  sense) noise

the added noise. In Figure 4 we plot a profile of the reconstructed curl  $C^{(1)}(x)$  (gray line) against the correct values (black line). (This plot corresponds to the cross-section of the third component of  $C^{(1)}$  along the line  $x_2 = 0.5$ ,  $x_3 = 0.5$ ). The latter figure shows that the noise is amplified during the first step (inversion of the spherical mean Radon transform). This is to be expected, since the corresponding inverse problem is mildly ill-posed (similarly to the classical inverse Radon transform). However, on the second step, corresponding to solving the problem (34), the noise is significantly reduced. This is not surprising, since the corresponding operator is a smoothing one. As a result, we obtain the low-noise image shown in Figure 1(b).

For the second simulation we used a phantom of  $\ln \sigma$  modeled by a linear combination of slightly smoothed characteristic functions of balls of different radii. The balls were centered on the pair-wise intersections of planes  $x_1 = 0.25$ ,  $x_2 = 0.25$ ,

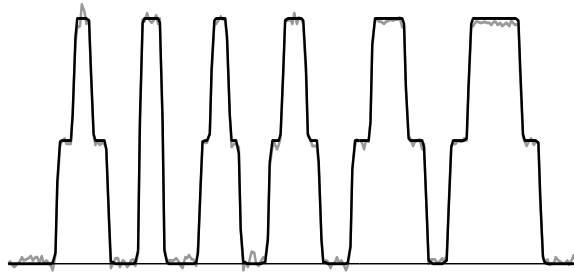


**Figure 8.** The cross section of the reconstructed image by the line  $x_1 = 0.25$ ,  $x_3 = 0.25$ . The thick black line represents the phantom, the gray line corresponds to the image reconstructed from the data with added 100% (in  $L^2$  sense) noise

$x_3 = 0.25$  (Figure 5). The minimum value of  $\ln \sigma$  in this phantom was 0 (black color), the maximum value is 1 (white color). The simulated data corresponded to the acoustic sources located at the nodes of  $257 \times 257$  Cartesian grids on each of the six faces of cubic domain  $\Omega$ . For each source, time series of 447 values for each measuring functional were simulated. The noise was modeled by adding to each time series a random sequence scaled so that the  $L^2$  norm of the noise was equal to that of the signal.

In Figure 6 we show the graph of  $M_{I,B^{(3)}}(y, t)$  for the point  $y = (1, 0.5, 0.5)$ . The black line represents the accurate data; the gray line shows the data with added noise.

The reconstruction was performed on  $257 \times 257 \times 257$  grid. The cross sections of the reconstructed image by planes  $x_1 = 0.25$  and  $x_2 = 0.25$  are shown in the Figure 7(b) and (d), next to the corresponding images of the phantom (i.e. parts (a) and (c) of the latter figure). The cross section profile of the image shown in part (d), corresponding to the line  $x_1 = 0.25$ ,  $x_3 = 0.25$ , is plotted in Figure 8.

As before, we obtained a very accurate reconstruction with little noise. This is again the result of the smoothing occurring when the Poisson problem is solved on the last step of the algorithm. Additionally, the image benefits from the singular nature of the phantom. While the noise is more or less uniformly distributed over the volume of the cubic domain, the signal (the non-zero  $\ln \sigma$ ) is supported in a rather small fraction of the volume, thus increasing the visual contrast between the noise and the signal.

We have also conducted a third numerical experiment with the the same phantom and the same discretization grid as in the second simulation. This time we reconstructed only two curls  $C^{(1)}$  and  $C^{(2)}$  and, further, computed only currents  $J^{(1)}$  and  $J^{(2)}$ . Instead of using formula (33) at each point of the discretization grid, we solved equations (37), (38) and (39) to obtain  $\nabla \ln \sigma$ . The rest of the algorithm was the same: compute  $\nabla \cdot \nabla \ln \sigma$  and solve the Poisson equation for  $\ln \sigma$ . The result of the reconstruction was practically indistinguishable from the one shown in Figure 7(b) and (d). While the level of noise in the image was slightly higher than in the previous simulation with three currents, it still was remarkably low.

## Final remarks and conclusions

### *Mathematical model*

In Section 1 we presented a mathematical model of the MAET measurements. In general, it agrees with the models [13, 30]. However, instead of point-wise electrical measurements we consider a more general scheme. The advantage of such an approach is generality and ease of analysis and numerical modeling. In particular, it contains as a particular case the pointwise measurement of electrical potentials (as in [13, 30]).

Another novel element in our model is the use of velocity potentials. It simplifies analysis and leads to a better understanding of the problem at hand. We discussed in detail the case of acoustic signal presented by propagating acoustic fronts from small sources. However, the same mathematics can be used to model time-harmonic sources. Since the problem is linear with respect to the velocity potential, the connection between the two problems is through the direct and inverse Fourier transforms of the data in time. Finally, plane wave irradiation (considered for example in [30]) is a partial case of irradiation by time harmonic sources, when they are located far away from the object.

### *General reconstruction scheme*

In Sections 2, 3, and 4 we presented a general scheme for solving the inverse problem of MAET under the assumption of propagating spherical acoustic fronts. (A slight modification of this scheme would allow one to utilize time harmonic sources and plane waves instead of the fronts we used). The scheme consists of the following steps:

- (i) Apply one of the suitable TAT reconstructions techniques to measuring functionals  $M_{I^{(k)}, B^{(j)}}(y, t)$ ,  $j, k = 1, 2, 3$ , to reconstruct the regular terms  $\frac{\partial}{\partial t} M_{I^{(k)}, B^{(j)}}^{\text{reg}}(x, 0)$  and thus to obtain the curls of  $J^{(k)}$ .
- (ii) Compute currents  $J^{(k)}$  from their curls (this step may require solving the Neumann problem for the Laplace equation)
- (iii) Find  $\nabla \ln \sigma$  at each point in  $\Omega$  using formula (33) or by solving system of equations (37), (38), (39).
- (iv) Find values of  $\Delta \ln \sigma$  by computing the divergence of  $\nabla \ln \sigma$ , and compute  $\ln \sigma$  by solving the Poisson problem with the zero Dirichlet boundary conditions.

Theoretical properties and numerical methods for all four steps are well known. The first step is mildly ill-posed (similar to the inversion of the classical Radon transform), the second and the third steps are stable, and the fourth step is described by a smoothing operator. Our rather informal discussion suggests that the total reconstruction procedure is stable (it does not exhibit even the mild instability present in classical computer tomography), and our numerical experiments confirm this assertion. We leave a rigorous proof of this conjecture for the future work.

### *Comparison with AEIT*

Similarly to AET, MAET overcomes the instability of EIT by combining the electrical measurements with ultrasound modulation. However, MAET has some advantages. First, the arising inverse problem is linear and can be solved explicitly. Secondly, the AEIT yields a very weak signal; successful acquisition of AET data in a realistic configuration have not been reported so far. The signal in MAET is stronger and first reconstructions from real data have already been obtained [13].

### *The case of a rectangular domain*

In Section 5 we presented a completely explicit set of formulae that yield a series solution of the MAET problem for the case of the cubic domain. It reduces the problem to a set of sine and cosine Fourier transforms, and thus, it can be easily implemented using FFTs. This, in turn, results in a fast algorithm that requires  $\mathcal{O}(n^3 \ln n)$  floating point operations to complete a reconstructions on a Cartesian grid with  $n^3$  nodes.

### *Feasibility of reconstruction using two directions of $B$*

It is theoretically possible to shorten the potentially long acquisition time by reducing the number of different directions of  $B$ . If only two orthogonal directions of magnetic field  $B$  are used, only two components of a curl  $C = \nabla \times J_I$  will be reconstructed on the first step of our method (say  $C_1$  and  $C_2$ ). However, since  $\operatorname{div} \operatorname{curl} J = 0$ ,

$$\frac{\partial}{\partial x_3} C_3 = -\frac{\partial}{\partial x_1} C_1 - \frac{\partial}{\partial x_2} C_2.$$

Since  $C$  vanishes on  $\partial\Omega$ , the above equation can be integrated in  $x_3$ , and thus  $C_3$  can be reconstructed from  $C_1$  and  $C_2$ . A further study is needed to see how much this procedure would affect the stability of the whole method.

### *Acknowledgements*

The author gratefully acknowledges support by the NSF through the grant DMS-0908208. We are also thankful to anonymous referees for numerous helpful suggestions.

## **Appendix**

Consider the following system of linear equations

$$\begin{cases} \mathbf{x} \cdot (\mathbf{a} \times \mathbf{b}) = R_1 \\ \mathbf{x} \cdot (\mathbf{a} \times \mathbf{c}) = R_2 \\ \mathbf{x} \cdot (\mathbf{b} \times \mathbf{c}) = R_3 \end{cases} \quad (44)$$

where  $\mathbf{a} = (a_1, a_2, a_3)^T$ ,  $\mathbf{b} = (b_1, b_2, b_3)^T$ , and  $\mathbf{c} = (c_1, c_2, c_3)^T$  are given linearly independent vectors in  $\mathbb{R}^3$ ,  $\mathbf{x} = (x_1, x_2, x_3)^T$  is the vector of unknowns, and  $R_1, R_2,$

$R_3$  are given numbers. Equations (44) can be re-written in the following form

$$R_1 = \begin{vmatrix} a_1 & b_1 & x_1 \\ a_2 & b_2 & x_2 \\ a_3 & b_3 & x_3 \end{vmatrix}, \quad R_2 = - \begin{vmatrix} a_1 & x_1 & c_1 \\ a_2 & x_2 & c_2 \\ a_3 & x_3 & c_3 \end{vmatrix}, \quad R_3 = \begin{vmatrix} x_1 & b_1 & c_1 \\ x_2 & b_2 & c_2 \\ x_3 & b_3 & c_3 \end{vmatrix}$$

or

$$v_1 = \frac{1}{\det A} \begin{vmatrix} a_1 & b_1 & x_1 \\ a_2 & b_2 & x_2 \\ a_3 & b_3 & x_3 \end{vmatrix}, \quad v_2 = \frac{1}{\det A} \begin{vmatrix} a_1 & x_1 & c_1 \\ a_2 & x_2 & c_2 \\ a_3 & x_3 & c_3 \end{vmatrix}, \quad v_3 = \frac{1}{\det A} \begin{vmatrix} x_1 & b_1 & c_1 \\ x_2 & b_2 & c_2 \\ x_3 & b_3 & c_3 \end{vmatrix}, \quad (45)$$

where  $A$  is a matrix whose columns are vectors  $\mathbf{a}$ ,  $\mathbf{b}$ , and  $\mathbf{c}$ ;  $v_j = \frac{R_j(-1)^{j+1}}{\det A}$ ,  $j = 1, 2, 3$ . Introduce vectors  $\mathbf{R} = (R_3, -R_2, R_1)^T$  and  $\mathbf{v} = (v_1, v_2, v_3)^T$ . Then formulae (45) can be viewed as the solution of the system of equations  $A\mathbf{v} = \mathbf{x}$  obtained using Cramer's rule. Therefore, solution of (44) is given by the formula

$$\mathbf{x} = A\mathbf{v} = \frac{1}{\det A} A\mathbf{R} = \frac{1}{\mathbf{a} \cdot (\mathbf{b} \times \mathbf{c})} A\mathbf{R}.$$

## References

- [1] M. Agranovsky and P. Kuchment, Uniqueness of reconstruction and an inversion procedure for thermoacoustic and photoacoustic tomography with variable sound speed, *Inverse Problems* **23** (2007) 2089–102.
- [2] G. Ambartsoumian and S. Patch, Thermoacoustic tomography: numerical results. Proceedings of SPIE 6437 *Photons Plus Ultrasound: Imaging and Sensing 2007: The Eighth Conference on Biomedical Thermoacoustics, Optoacoustics, and Acousto-optics*, (2007) Alexander A. Oraevsky, Lihong V. Wang, Editors, 64371B.
- [3] H. Ammari, E. Bonnetier, Y. Capdeboscq, M. Tanter, and M. Fink, Electrical impedance tomography by elastic deformation, *SIAM J. Appl. Math.* **68** (2008) 1557–1573.
- [4] H. Ammari, Y. Capdeboscq, H. Kang, and A. Kozhemyak, Mathematical models and reconstruction methods in magneto-acoustic imaging, *Euro. Jnl. of Appl. Math.*, **20** (2009) 303–17.
- [5] D. C. Barber, B. H. Brown, Applied potential tomography, *J. Phys. E.: Sci. Instrum.* **17** (1984), 723–733.
- [6] L. Borcea, Electrical impedance tomography, *Inverse Problems* **18** (2002) R99–R136.
- [7] P. Burgholzer, G. J. Matt, M. Haltmeier, and G. Paltauf, Exact and approximative imaging methods for photoacoustic tomography using an arbitrary detection surface, *Phys Review E*, **75** (2007) 046706.
- [8] Y. Capdeboscq, J. Fehrenbach, F. de Gournay, O. Kavian, Imaging by modification: numerical reconstruction of local conductivities from corresponding power density measurements, *SIAM J. Imaging Sciences*, **2/4** (2009) 1003–1030.
- [9] M. Cheney, D. Isaacson, and J. C. Newell, Electrical Impedance Tomography, *SIAM Review*, **41**, (1999) 85–101.
- [10] D. Colton and R. Kress, *Inverse acoustic and electromagnetic scattering theory*, Springer-Verlag (2001).
- [11] D. Finch, S. Patch and Rakesh, Determining a function from its mean values over a family of spheres, *SIAM J. Math. Anal.*, **35** (2004) 1213–40.
- [12] D. Gilbarg and N. S. Trudinger, *Elliptic Partial Differential Equations of Second Order*, Springer-Verlag (1983).

- [13] S. Haider, A. Hrbek, and Y. Xu, Magneto-acousto-electrical tomography: a potential method for imaging current density and electrical impedance, *Physiol. Meas.* **29** (2008) S41-S50.
- [14] Y. Hristova, P. Kuchment, and L. Nguyen, On reconstruction and time reversal in thermoacoustic tomography in homogeneous and non-homogeneous acoustic media, *Inverse Problems*, **24**: 055006, 2008.
- [15] R. A. Kruger, P. Liu, Y. R. Fang, and C. R. Appledorn, Photoacoustic ultrasound (PAUS) reconstruction tomography, *Med. Phys.*, **22** (1995) 1605–09.
- [16] R. A. Kruger, D. R. Reinecke, and G. A. Kruger, Thermoacoustic computed tomography - technical considerations, *Med. Phys.* **26** (1999) 1832–7.
- [17] P. Kuchment and L. Kunyansky, Mathematics of Photoacoustic and Thermoacoustic Tomography, Chapter 19, *Handbook of Mathematical Methods in Imaging*, Springer-Verlag, (2011) 819-865.
- [18] P. Kuchment and L. Kunyansky, Synthetic focusing in ultrasound modulated tomography, *Inverse Problems and Imaging*, **4** (2010) 665 – 673.
- [19] P. Kuchment and L. Kunyansky, 2D and 3D reconstructions in acousto-electric tomography, *Inverse Problems* **27** (2011) 055013.
- [20] L. Kunyansky, Explicit inversion formulae for the spherical mean Radon transform, *Inverse Problems*, **23** (2007) 737–783.
- [21] L. Kunyansky, A series solution and a fast algorithm for the inversion of the spherical mean Radon transform, *Inverse Problems*, **23** (2007) S11–S20.
- [22] L. Kunyansky, Reconstruction of a function from its spherical (circular) means with the centers lying on the surface of certain polygons and polyhedra, *Inverse Problems*, **27** (2011) 025012.
- [23] L. Kunyansky, Fast reconstruction algorithms for the thermoacoustic tomography in certain domains with cylindrical or spherical symmetries, Preprint (2011) Arxiv:Math.AP 1102.1413
- [24] L. Kunyansky and P. Kuchment, Synthetic focusing in Acousto-Electric Tomography, in *Oberwolfach Report* No. 18/2010 DOI: 10.4171/OWR/2010/18, Workshop: Mathematics and Algorithms in Tomography, Organised by Martin Burger, Alfred Louis, and Todd Quinto, April 11th – 17th, (2010) 44–47.
- [25] B. Lavandier, J. Jossinet and D. Cathignol, Experimental measurement of the acousto-electric interaction signal in saline solution, *Ultrasonics* **38** (2000) 929–936.
- [26] A. Montalibet, J. Jossinet, A. Matias, and D. Cathignol, Electric current generated by ultrasonically induced Lorentz force in biological media, *Med. Biol. Eng. Comput.* **39** (2001) 15–20.
- [27] S. J. Norton and M. Linzer, Ultrasonic reflectivity imaging in three dimensions: exact inverse scattering solutions for plane, cylindrical, and spherical apertures, *IEEE Trans. on Biomed. Eng.*, **28** (1981) 200–202.
- [28] L. Nguyen, A family of inversion formulas in thermoacoustic tomography, *Inverse Problems and Imaging*, **3** (2009) 649–675.
- [29] A. A. Oraevsky, S. L. Jacques, R. O. Esenaliev, and F. K. Tittel, Laser-based photoacoustic imaging in biological tissues, *Proc. SPIE*, **2134A** (1994) 122–8.
- [30] B. J. Roth and K. Schalte, Ultrasonically-induced Lorentz force tomography, *Med. Biol. Eng. Comput.* **47** (2009) 573–7.
- [31] A. M. Stewart, Longitudinal and transverse components of a vector field, *Classical Physics*. In press, <http://arxiv.org/abs/0801.0335v2>.
- [32] V. S. Vladimirov, *Equations of mathematical physics*. (Translated from the Russian by Audrey Littlewood. Edited by Alan Jeffrey.) Pure and Applied Mathematics, **3** Marcel Dekker, New York (1971).
- [33] Wang L V (Editor) 2009 *"Photoacoustic imaging and spectroscopy"* (CRC Press).
- [34] H. Wen, J. Shah, R. S. Balaban, Hall effect imaging, *IEEE Trans. Biomed. Eng.*, **45** (1998) 119–24.
- [35] M. Xu and L.-H. V. Wang, Time-domain reconstruction for thermoacoustic tomography in a spherical geometry, *IEEE Trans. Med. Imag.*, **21** (2002) 814–822.
- [36] H. Zhang and L. Wang, Acousto-electric tomography, *Proc. SPIE* **5320** (2004) 145–9.